Draft version December 29, 2017
Preprint typeset using LaTeX style emulateapj v. 12/16/11

DRESSING THE CORONAL MAGNETIC EXTRAPOLATIONS OF ACTIVE REGIONS WITH A PARAMETERIZED THERMAL STRUCTURE

Gelu M. Nita[1], Nicholeen M. Viall[2], James A. Klimchuk[2], Maria A. Loukitcheva[1,4], Dale E. Gary[1], Alexey A. Kuznetsov[3], Gregory D. Fleishman[1]

Draft version December 29, 2017

ABSTRACT

The study of time-dependent solar active region morphology and its relation to eruptive events requires analysis of imaging data obtained in multiple wavelength domains with differing spatial and time resolution, ideally in combination with 3D physical models. To facilitate this goal, we have undertaken a major enhancement of our IDL-based simulation tool, `GX_Simulator`, previously developed for modeling microwave and X-ray emission from flaring loops, to allow it to simulate quiescent emission from solar active regions. The framework includes new tools for building the atmospheric model, and enhanced routines for calculating emission that include new wavelengths. In this paper, we use our upgraded tool to model and analyze an active region and compare the synthetic emission maps with observations. We conclude that the modelled magneto-thermal structure is a reasonably good approximation of the real one.

Subject headings: Sun: flares–acceleration of particles–turbulence–diffusion–Sun: magnetic fields–Sun: radio radiation

1. INTRODUCTION

Understanding solar activity, which consists of an inter-related set of complex physical phenomena occurring in multiple layers of the solar atmosphere, is a primary goal of solar physics. The main driver of solar activity, the solar magnetic field, is generated by the solar dynamo action at the bottom of the convective zone. Then, the magnetic flux tubes rise due to magnetic buoyancy and emerge from the sub-photospheric solar interior to form the sunspots and active regions (ARs). In these strong-field regions, the magnetic pressure in the corona dominates over the kinetic pressure and so controls the cross-field plasma dynamics.

Modeling an active region for quantitative comparison with data is extremely challenging. Even assuming that an active region can be modeled as a quasi-static system, the three-dimensional modeling of the spatially complex solar atmosphere must be addressed, and one must include a quantitative treatment of the full suite of data that are available. In addition, a series of such quasi-static models is needed to represent the time dynamic evolution of ARs. This is necessary for studying the onset conditions for solar flares, coronal mass ejections (CMEs), and is likely important even for evolving quiescent conditions. Here we advance this enormously challenging problem by developing an easy-to-use, and relatively fast modeling framework based on both observations and well-developed modeling elements such as nonlinear force-free field (NLFFF) extrapolations and zero-dimensional (0D) hydrodynamic heating models. To develop and validate this framework, we have extended our IDL-based simulation tool available as the `GX_Simulator` package within the SolarSoft, which was previously developed for modeling microwave and X-ray emission from flaring loops (Nita et al. 2015).

The object-based architecture, which runs on Windows, Mac and Linux platforms, provides an interactive graphical user interface that allows the user to import photospheric magnetic field maps as input to the magnetic field extrapolations within the tool, or alternatively to import 3D numerical magnetic field models created externally by any means, such as NLFFF extrapolations or dynamic (data-driven or full-fledged MHD) models. The magnetic framework is then populated by importing a 3D density and temperature distribution model, or alternatively assigning to each individual volume element (voxel) numerically defined differential emission measure (DEM) distributions from parametric heating models involving averaged properties of the magnetic field lines crossing a given voxel. The spatial and spectral properties of radio, EUV and X-ray emission from the model are then calculated within the tool, and the model-derived images and spectra can then be compared with observational data imported into the tool. The application integrates shared-object libraries containing fast microwave (gyrosynchrotron and gyroresonance) emission codes developed in FORTRAN and C++, soft and hard X-ray and EUV codes developed in IDL, a FORTRAN-based potential-field extrapolation routine (method of scalar potential, Abramenko 1986) and an IDL-based linear force-free field extrapolation routine (Selhorst et al. 2005) following the fast Fourier method proposed by Alissandrakis (1981). We have also added to the `GX_Simulator` distribution package an almost fully automated way of downloading needed SDO maps, producing NLFFF reconstruction using

[1] Center For Solar-Terrestrial Research, New Jersey Institute of Technology, Newark, NJ 07102, USA
[2] NASA Goddard Space Flight Center, Greenbelt, MD 20771, USA
[3] Institute of Solar-Terrestrial Physics, 126a Lermontov Str., Irkutsk 664033, Russia
[4] Saint Petersburg State University, 7/9 Universitetskaya nab., St. Petersburg, 199034 Russia

the weighted optimization code described and tested by Fleishman et al. (2017), and dressing the NLFFF data cube with the thermal plasma as described in the remainder of the paper. The interactive interface allows users to add any user-defined IDL or externally-callable radiation code that adheres to our simple interface standards, as well as user-defined magnetic field extrapolation routines. Here we describe this tool and demonstrate its use to model an AR and compare the synthetic emission maps obtained in different wavelengths with observations.

2. APPROACHES TO AR MODELING

A direct approach to AR modeling would be the creation of a single, 'do-it-all' radiative MHD/kinetic model, which would describe formation and detailed evolution of ARs from first principles. This approach would have the advantage of solving self-consistently for the magnetic field structure and plasma distribution. However, such an approach is a research area by itself, and is not appropriate to the general interpretation of observations that is of interest to the vast majority of researchers. The first-principles approach is also too computationally expensive for daily use, and is itself necessarily approximate, generally requiring knowledge of the sub-photospheric velocity and magnetic field that are not directly accessible by available observational techniques. Although our modeling tool allows importing such externally-generated models, from which it calculates various emissions for comparison with observations, in this paper we demonstrate an alternative method of creating a model that is more general and likely to be of wider practical use.

A useful approximation is a so-called "data-driven" modeling approach, in which the magnetic field and plasma, each constrained by observational data, are treated separately. This is believed to be valid in the regions of the solar corona producing the bulk of the EUV, X-ray, and microwave emissions used for comparison, due to the dominance of magnetic pressure there (the low-plasma-beta condition $\beta \ll 1$, where $\beta = 8\pi nkT/B^2$ is the ratio of plasma pressure to magnetic pressure, Gary 2001). In this approximation, a set of simplified MHD equations is solved for the corona, with the evolving boundary conditions obtained from observations of the photospheric boundary.

A further simplification of this approach is a static approximation that ignores all plasma effects except for the electric current. This modeling has come to be known as NLFFF reconstructions (extrapolations). An extrapolation for a given time results in a static magnetic field structure without any thermal plasma structure. This modeling approach is capable of tracking the magnetic field evolution, but only by means of a time series of such static models.

2.1. *Coronal Magnetic Field Reconstructions*

In the low-β corona, plasma and thermally-conducted energy flow along the magnetic field, but not across it. The field acts essentially like a collection of rigid, thermally insulated flow pipes. This implies that we can start building our coronal model from constructing the magnetic field "skeleton," which later will be populated with the thermal pasma. A static solution for the magnetic field in the low-β corona represents a force-free configuration, which can be approximately restored using a boundary condition. In practice, vector fields are measured from full-Stokes polarized intensity of Zeeman sensitive spectral lines with circular polarization providing line-of-sight field strength and linear polarization providing the transverse field. Then, to obtain the field away from the boundary, the measured photospheric fields are extended into the corona through potential or force-free field extrapolations. Starting with Sakurai (1981), these extrapolations nowadays have reached a high level of sophistication (see reviews by Sakurai 1989; Amari et al. 1997; Wiegelmann 2008). Routine magnetic field extrapolations are now available using the best optical data yet: the high-resolution, full-disk vector magnetic field measurements from the Helioseismic and Magnetic Imager (HMI) onboard the Solar Dynamics Observatory (SDO) (Scherrer et al. 2012).

These extrapolations, although ignoring the influence of plasma pressure, correctly reproduce many important properties of the corona above ARs: magnetic structures built using such extrapolations can often match some of the chromospheric Hα fibrils (Jing et al. 2010), coronal loops illuminated by EUV or SXR emission (Malanushenko et al. 2009; Tadesse et al. 2014), or spatial locations of the microwave gyroresonance (GR) sources (Nita et al. 2011). Using an available outcome of a full-fledged MHD model, Fleishman et al. (2017) showed that the NLFFF reconstruction tools faithfully reproduce the original dynamical model within appropriate statistical errors, which validates the use of NLFFF reconstructions for coronal modeling. Currently, we are using the weighted optimization coded ("AS code," see Fleishman et al. 2017, for definitions and details) complied from the C++ source code as a callable library as the default one in the `GX_Simulator` package. The library of the NLFFF reconstruction codes will be enlarged in the future following the modeling needs.

Similarly, a time-dependent magnetic data cube obtained from the data-driven modeling can be utilized. In summary, a number of observation-based methods are available to build a realistic 3D cube of the vector magnetic field for a given AR at a given time. Below, we use one instance of such a data cube corresponding to AR11072, which was obtained using the NLFFF extrapolation technique applied to vector magnetogram data obtained by HMI on 23-May-2010 at 11:58:24.700 UT.

2.2. *Populating the Extrapolated Magnetic Data Cube with a Thermal Plasma*

Electromagnetic emission produced by free electrons, ions, atoms, or molecules is observed in various wavelength domains. However, as has been noted above, a quasi-static (NLFFF) model is only a skeleton that does not include a self-consistent thermal coronal model responsible for such emissions. We have to artificially supply our 3D magnetic data cube

with a thermal distribution to consistently model the observed emissions. Because of the strong anisotropy of kinetic processes in the strong magnetic field case (e.g. Fleishman & Toptygin 2013), the thermal model must be closely linked with the original magnetic skeleton. The skeleton forms the individual field lines (flux tubes) guiding thermal conduction, which in turn is largely responsible for the thermal distribution of plasma. To take the guiding magnetic field structure into account, we assume that each magnetic flux tube can be treated as an elementary thermal object, whose thermal structure can differ for open and closed field lines. As detailed below, we employ a heating model for the closed field lines that depends on the magnetic loop length, mean magnetic field strength, and, in principle, the electric current (force-free parameter α, which is theoretically constant along any field line in a force-free field configuration). Since the flux tube length is undefined for open fields, our model assumes no heating on those field lines and instead imposes a barometric thermal model.

2.3. *Coronal Heating Models*

There are three main approaches to modeling coronal heating. As noted above, one is the global MHD approach, where modelers use first-principles to simulate entire ARs or large portions thereof (e.g., Gudiksen & Nordlund 2005; Peter et al. 2006; Hansteen et al. 2010; Rempel & Cheung 2014). In such models, the footpoints of coronal field lines are driven by motions that represent photospheric convection or other flows, and coronal heating is computed self-consistently from the equations without an ad hoc heating term. The disadvantage of this approach is that some essential coronal microphysics is not captured. For example, the many current sheets that are expected to be present are highly under-resolved. Consequently, the process by which magnetic energy is converted into heat in the corona is treated unrealistically.

A second approach models the local MHD or kinetic physics at a single energy release site, a current sheet for example, and attempts to resolve as much of the fundamental structure and dynamics as possible (e.g., Dahlburg et al. 2005; Daughton et al. 2009). Though the energy conversion process is treated as accurately as possible, the important connection between large and small scales is either missing or treated artificially. Additionally, the important energetic and dynamic coupling between the corona and lower atmosphere is not included. This coupling controls the processes of chromospheric evaporation and condensation, without which it is impossible to accurately describe the evolution of the plasma and the observational signatures of the heating. The resulting models cannot be readily tested or compared with observations.

Ideally, one would combine these two approaches into a single self-consistent model, but this is far beyond the computational capabilities at present or in the foreseeable future. Instead, we use here a synthetic approach based on complementary modeling elements: 3D magnetic extrapolations (e.g., a NLFFF data cube), and field-aligned hydrodynamic models with assumed heating along the individual magnetic flux tubes defined by the extrapolated field line structure. The hydrodynamic simulation code that we use is called Enthalpy-Based Thermal Evolution of Loops (EBTEL; Klimchuk et al. 2008; Cargill et al. 2012a,b), which includes the important link between the corona and lower atmosphere in order to realistically model the plasma response to coronal heating.

Given an assumed heating profile (time-dependent heating rate), the response of the plasma is modeled in the context of field-aligned hydrodynamics, taking full account of chromospheric evaporation and condensation (Klimchuk 2006, and references therein). The code is zero dimensional in the sense that it computes the evolution of the average temperature, density, and pressure, where the averaging is taken along the coronal portion of the magnetic strand. Taking the coronal average is reasonable, because thermal conduction and flows are very efficient at smoothing out field-aligned gradients. Gradients are very steep in the transition region, on the other hand, and EBTEL computes the instantaneous differential emission measure distribution, DEM(T), of the transition region footpoints. EBTEL provides an excellent approximation to more sophisticated 1D codes, but using $10^3 - 10^4$ times less computing time. This gives the user the ability to rapidly examine a large range of parameter space. The EBTEL code is broadly applicable and is now being widely used by the solar community.

3. BUILDING A THERMAL STRUCTURE ONTO THE MAGNETIC SKELETON

Following §2.1, we obtain an equilibrium coronal magnetic field model, which we then populate with a thermal plasma using a given heating model. The thermal plasma parameters are obtained from the EBTEL hydrodynamic model, which includes heat conduction, enthalpy, and radiation. The volumetric heating rate is the parameter of principal importance in defining the thermal structure of a flux tube. Theoretical considerations suggest that the volumetric heating rate should have a power-law dependence on the magnetic field strength (B), field line length (L), and, in some cases, plasma density (ρ). Different theories predict different value for the power-indices, as discussed fully in Mandrini et al. (2000) and references therein. For this study, we adopt indices appropriate to a scenario in which the coronal magnetic field is stirred by random footpoint motions associated with photospheric convection. Stresses and magnetic energy are released by reconnection with the angle between adjacent magnetic strands reaches a critical value (e.g., Dahlburg et al. 2005). We are not claiming that this is necessarily the way in which coronal heating works on the Sun. It is simply the model we have chosen to use to test our improvements to the `GX_Simulator`. A future goal is to try many different coronal heating models, each with a different set of power-law indices, to see which best reproduces actual observations.

In contrast to coronal heating, cooling processes are well understood; in a general case they include the radiative losses and the field-aligned transfer of

the mass, momentum, and energy, which includes interaction with the high-density chromosphere resulting in the evaporations and condensations. This section presents the methodology of creating the thermal structure of the AR model. We describe how we "dress" the (3D) coronal magnetic skeleton with thermal plasma structures obtained from different EBTEL models (steady or impulsive heating).

3.1. *Thermal Structure of a Given Volume Element*

To populate the magnetic data cube with a thermal plasma distribution, we have to assign the thermal information (either in the form of densities and temperatures or in the form of DEM) to each elementary volume element (hereafter voxel). At the same time, the structure resulting from the highly anisotropic transport processes in the magnetized solar corona, in particular the heat transfer which occurs primarily along the magnetic field lines (e.g. Fleishman & Toptygin 2013), must be preserved. From this perspective it is reasonable to consider the plasma heating and cooling processes in 1D structures aligned with the field lines defined by the 3D structure–magnetic flux tubes. The net result for a given voxel will strongly differ depending on whether it is attached to an open or closed flux tube, as well as on the length and mean magnetic field of the given flux tube, as described above.

3.2. *Heating a Given Flux Tube*

Here we describe a reasonably general framework applicable to the heating of a given flux tube modeled as a field-aligned plasma cylinder. To do so, we note that all coronal heating mechanisms, including wave heating, generally result in impulsive energy release on individual flux tubes (Klimchuk 2006, 2015). The term "steady" coronal heating implies that the repeat time of the heating events, τ, is much shorter than the cooling time of the plasma. For simplicity, we refer to impulsive heating events as nanoflares. We must specify the duration Δt of the nanoflares, and the time interval between successive events within the same strand, τ. The volumetric heating rate is therefore given by

$$Q(t) = Q_0 \left(\frac{B}{B_0}\right)^a \left(\frac{L}{L_0}\right)^b f(t), \qquad (1)$$

where the heating profile $f(t)$ incorporates τ and Δt, and it may also incorporate the effect of the density ρ.

There are thus five independent parameters: Q_0, a, b, τ, and Δt. Q_0 is a typical heating rate, which can depend on the driver velocity v and the electric current density along the flux tube, or, equivalently, on the force-free parameter α, and so it can be different for different flux tubes. The actual numerical value of Q_0 (measured in erg cm^{-3} s^{-1}) depends on the normalization constants, which we conveniently choose as $B_0 = 100$ G and $L_0 = 10^9$ cm. The power-law indices, a and b, have certain values for a given heating model; for example $a = 2$ and $b = -1$ within the *critical shear angle model* (Mandrini et al. 2000), which we will adopt as default parameters. The time constants τ and Δt are the free parameters of the model. In the proof-of concept model shown here, they are determined empirically based on analysis of the EUV AR lightcuves (Viall & Klimchuk 2012) and EBTEL modeling of these line-of-sight-integrated light curves (Viall & Klimchuk 2013). EBTEL is capable of accurately simulating the entire range of τ, from effectively "steady," to fully "impulsive" (see § 4.1 and Appendix A for more details).

Currently, the remaining input of Equation (1), Q_0, is under-constrained. In fact, the lack of a realistic choice for the heating rate Q_0 for a given flux tube remains the main limitation for the adopted heating approach, as this parameter is responsible for the selective flux tube heating; hence it is needed to reproduce the distinct loops routinely seen in EUV images, as we demonstrate below. For now we will treat Q_0 as a phenomenological parameter depending, at most, on the force-free α parameter computed locally from the magnetic data cube itself. However, in principle, it can further be constrained from consideration of the chromospheric/photospheric driver velocities available from an MHD model, or from other chromospheric data including UV and IR lines and photospheric Dopplergrams.

3.3. *Populating the Coronal Volume with a Thermal Model*

A challenge, which calls for a conventional choice of how exactly to attach the heating model to the (Cartesian) 3D magnetic skeleton, is that the heating model applies to a magnetic flux tube–a curved object covering a non-Cartesian set of voxels. In many publications comparing heated flux tubes and EUV coronal loops, the flux tubes are formed manually, e.g., starting from a number of manually chosen photospheric pixels and then extrapolating the field lines into the corona (e.g., Ugarte-Urra et al. 2017). This way only a small subset of voxels (tracing the manually selected flux tubes) are "selectively heated" instead of treating all the voxels objectively, and many coronal voxels remain empty.

To address this volume filling problem, we formulate the following algorithm. For each voxel we compute a characteristic field line passing through the center of the voxel. Then, we categorize the field lines into two groups–field lines that are closed (the field line starts and ends at the bottom boundary of the magnetic data cube) or open (the field line leaves the cube through a side or top boundary). If the given voxel is associated with an open field line, it is filled with pre-defined isothermal hydrostatic coronal plasma. For a voxel associated with a closed field line, we compute the field line length L and mean magnetic field along the line $B_{\rm mean}$. These two parameters are linked to this given voxel and stored with it. This procedure is repeated for all voxels of the data cube. In this way, a new 3D model is created, in which every voxel generating a closed field line is tagged with the parameters needed to apply a parametric heating model to this voxel according to Equation (1).

The number of voxels to be populated through this procedure by thermal plasma can be very large (about 10^7 or more), thus, applying the heating code to each field line is impractical. Instead, we run the EBTEL

hydrodynamic code to pre-compute several thousand combinations of flux tube lengths and nanoflare magnitudes. For each combination, we time average over the entire simulation, thereby producing two differential emission measure (DEM) distributions–one for the coronal portion of the loop and one for the transition region. The idea is that each loop is actually a bundle of much thinner strands that are heated at random times by identical nanoflares. The time average of one strand is deemed to be equivalent to a snapshot of many out-of-phase strands. We create a lookup table that contains the coronal and transition region DEM distributions for each pair of flux tube length and nanoflare magnitude. Knowing $B_{\rm mean}$ and L for a given coronal or transition region voxel, Equation (1) tells us the nanoflare magnitude, and we find the corresponding DEM distribution from the lookup table using a 4-closest-neighbor weighted interpolation. We have confirmed that this interpolation approach is nearly as accurate as one considering each field line individually, and thus it is a convenient compromise to efficiently populate the magnetic data cube with heated plasma.

Finally, some emission computations, e.g. microwave, do not require as detailed information as contained in the DEM distributions. To facilitate the later computation of microwave emission, we also compute an effective number density and temperature of the plasma from the DEM distribution moments,

$$n_{\rm eff} = \left(\int {\rm DEM}(T)\, {\rm d}T \right)^{1/2}, \qquad (2)$$
$$T_{\rm eff} = \frac{\int T \cdot {\rm DEM}(T)\, {\rm d}T}{n_{\rm eff}^2}.$$

We use these ($n_{\rm eff}$, $T_{\rm eff}$) pairs as input for radiation transfer codes, which we developed specifically for inclusion into the tool following theory developed by Fleishman & Kuznetsov (2014), and also for visualization within the tool.

We emphasize that the algorithm does not assign DEM tables or ($n_{\rm eff}$, $T_{\rm eff}$) pairs, but pairs of generic (hydrostatic) (n, T) values to those voxels intersected by open field lines, which may include field lines that are physically closed, but cross the model volume boundaries before reaching one of their footpoints.

3.4. *Populating the Chromospheric Volume*

The general approach we employ to populate the chromospheric volume is based on typical observationally established thresholds, which are used to distinguish quiet-Sun (QS) and AR features at the photospheric level, and on a set of one-dimensional solar atmospheric models of those features, which are used to fill the chromospheric volume. The atmospheric model set used in the current implementation of the `GX_Simulator` is essentially that of Fontenla et al. (2009). We distinguish between seven solar atmospheric brightness features. They include three QS components, namely internetwork (IN), network lane (NW), and enhanced network (ENW), and four AR features: sunspot umbra (UMB), penumbra (PEN), plage (PL), and facula (FA).

The temperature, electron and atomic hydrogen density profiles, as well as the ionization fraction corresponding to these one-dimensional models are illustrated in Figure 1. `GX_Simulator` computes these profiles using model-dependent variable-height steps that properly resolve the transition region (TR) layer. Consequently, the maximum height up to which a given chromospheric model profile is computed corresponds to a specific TR height ranging from $\sim 1000 - 2000$ km, which includes $65 - 90$ grid steps in our model.

As the photospheric input for choosing among the seven chromospheric models at each base voxel, `GX_Simulator` uses two standard SDO/HMI products: white light continuum limb-darkening-corrected filtergrams and HMI line-of-sight (LOS) magnetograms. However, to properly take into account the angle between the LOS direction and the direction of the local normal to the Sun's surface along which the extrapolation is performed (externally or in the `GX_Simulator` tool), these original images are transformed using the same Carrington-Heliographic or Helioprojective-Cartesian projection (Thompson 2006). These coordinate transformations assure that, when the model is placed in the proper 3D orientation relative to the observer, the base maps are projected onto their LOS counterparts with minimum distortion.

Using these projected magnetograms, we separate the non-magnetic QS voxels from the magnetic voxels based on an empirically chosen magnetogram threshold of 10 G. From the QS voxels we determine the mean white-light intensity $I_{\rm QS}$. Further subdivision of both QS and AR features is done relative to $I_{\rm QS}$. The intensity thresholds for the umbral (UMB) and penumbral (PEN) model components use thresholds of, respectively, 0.65 and 0.90 of $I_{\rm QS}$ following Mathew et al. (2007).

For the non-magnetic QS features we employ the thresholds provided in Fontenla et al. (2009). We derive two basic cut-off values, Th_B and Th_F, corresponding to 0.75 and, respectively, 0.97 of the cumulative white-light histogram, excluding sunspots. We classify the pixels between these cut-off values as NW type, and we consider all pixels with photospheric continuum intensity exceeding 90% of $I_{\rm QS}$ and less than Th_B as being of IN type. If white-light intensity is greater than Th_F and less than 119% of I_{QS}, we assign such pixels as being of ENW type. We determine the PL and FA components by combining the magnetogram and white-light intensities. We empirically set the magnetic thresholds as indicated below, while we adopt the white-light intensity thresholds from Fontenla et al. (2009). In particular, we assign to the PL type to all pixels with white-light intensity that exceeds 95% of $I_{\rm QS}$ and is less than Th_F, and with corresponding unsigned magnetogram signal greater than 30 G. The FA component encompasses pixels with white-light intensity greater than 101% of $I_{\rm QS}$ and unsigned magnetogram signal exceeding 30 G. Consequently, each pixel is classified as belonging to one of the seven photospheric features, and a corresponding pixel mask is created. An example of the resulting mask encompassing all seven

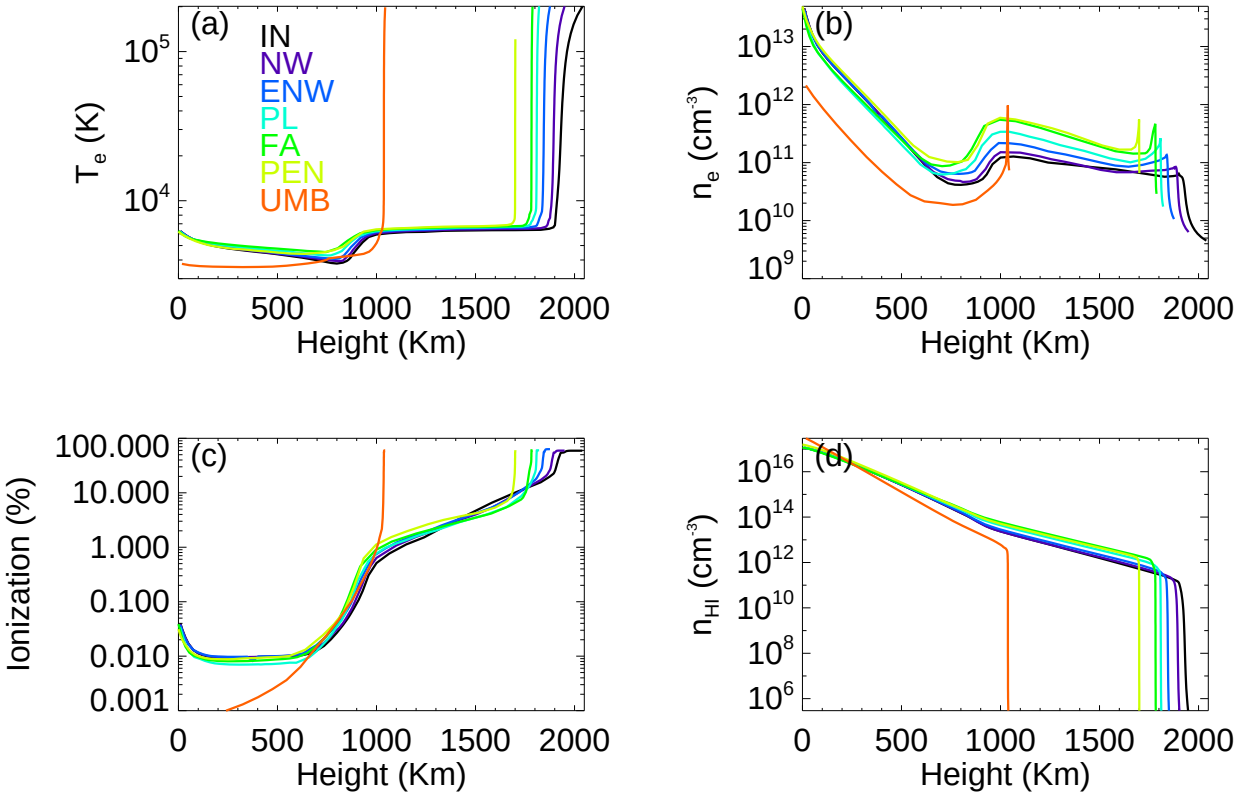

FIG. 1.— Height profiles of (a) temperature, (b) electron density, (c) ionization fraction, and (d) atomic hydrogen (HI) density, corresponding to seven color-coded (legend on panel a) chromospheric models used by the `GX_Simulator` to populate the chromospheric volume, i.e. internetwork (IN), network lane (NW), enhanced network (ENW), sunspot umbra (UMB), penumbra (PEN), plage (PL), and facula (FA).

components is shown in Figure 2, in the case of AR 11072 used for illustration in this study.

The mask displayed in Figure 2c, which has been constructed based purely on the photospheric HMI observational inputs displayed in panels 2(a,b), demonstrates a remarkable morphological agreement with the temperature-minimum/chromospheric image shown in Figure 2(d), which has been captured in the 1700 Å passband by the Atmospheric Imaging Assembly (AIA, Lemen et al. 2012) on board SDO. This justifies our use of the photospheric images as a basis for the chromospheric part of the model atmosphere, and validates the algorithm we employ to populate a chromospheric volume.

The `GX_Simulator` package includes a tool for applying the above selection thresholds automatically, and thus produces the corresponding chromospheric model based on a given HMI filtergram and LOS magnetogram pair. Thus, using the model mask computed by these means, `GX_Simulator` generates a chromospheric volume consisting of a collection of variable height (number of grid-steps) vertical columns, each corresponding to one of the seven chromospheric models associated with the photospheric mask pixel onto which such a column is projected.

3.5. *Connecting the Chromospheric and Coronal Models*

The final step in the process of building the thermal structure on top of the magnetic skeleton requires a means to handle the interface between the variable-height chromospheric model and the EBTEL-based coronal/TR model. The solution used in the current implementation of our modeling tool is to replace the bottom layers of the uniformly spaced magnetic skeleton with a composite slab having the minimum thickness needed to contain the variable height chromosphere.

For example, in the case of the NLFFF magnetic skeleton built for AR11072 using a typical observational resolution of 2″ (∼ 1500 km), such composite slab needs to have a thickness of ∼3000 km corresponding to the bottom two layers of the uniform extrapolation volume, while the height of the chromospheric column having the maximum number of 90 layers is ∼2000 km. Therefore, we divide the composite slab into 91 layers with non uniform heights, adding one or more extra voxels to account for uneven heights of the different chromospheric models as explained below. Each vertical column of the slab is assigned with the nonuniform heights corresponding to the bottom model mask up to the corresponding TR layers, while uniform heights are assigned to the remaining voxels of each column, such as to preserve the uniform ∼3000 km thickness of the composite slab and the integrity of the entire magnetic skeleton it is part of. Subsequently, we perform an irregular grid interpolation of the magnetic field along each vertical column of the slab, and transfer all physical properties from the original chromospheric and EBTEL-based coronal models to the newly created composite data cube.

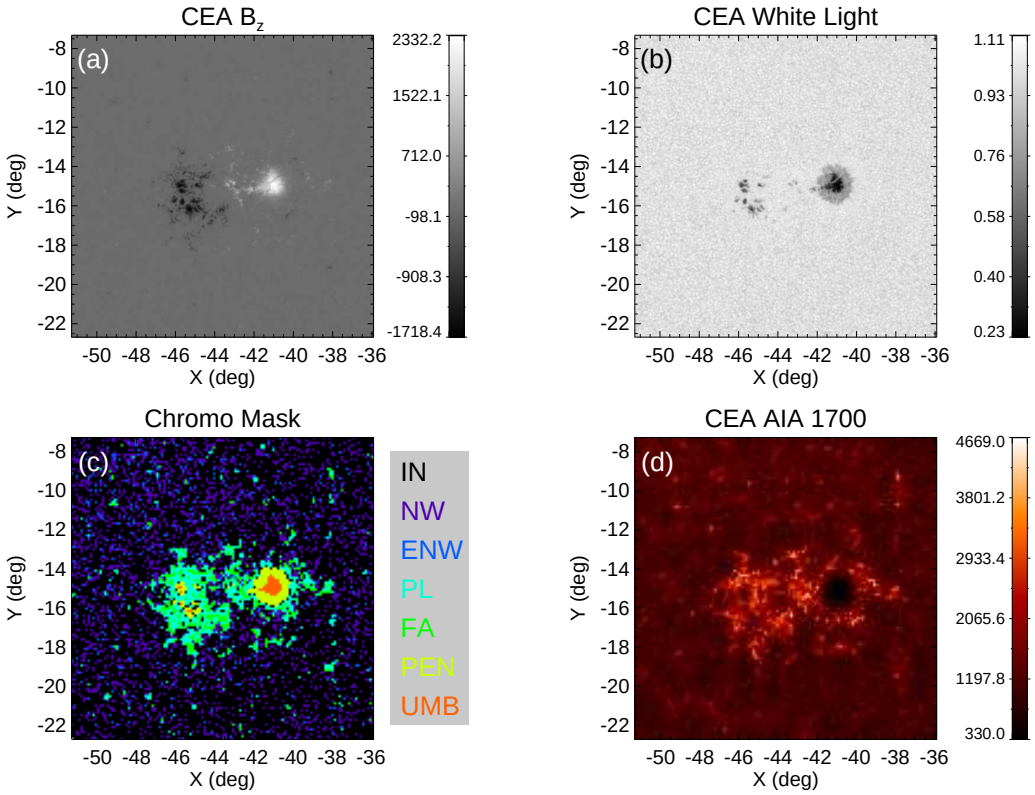

FIG. 2.— Chromospheric model mask creation for AR 11072 on 23-May-2010 11:58:25 UT. a) CEA projected B_z magnetic field strength. b) CEA projected HMI continuum intensity. c) Model mask comprising 7 color-coded components used to assign chromospheric models for each set of LOS chromosphere voxels projected onto a given mask pixel. d) CEA projected AIA 1700 Å image demonstrating a remarkable structural agreement with the mask depicted in panel c.

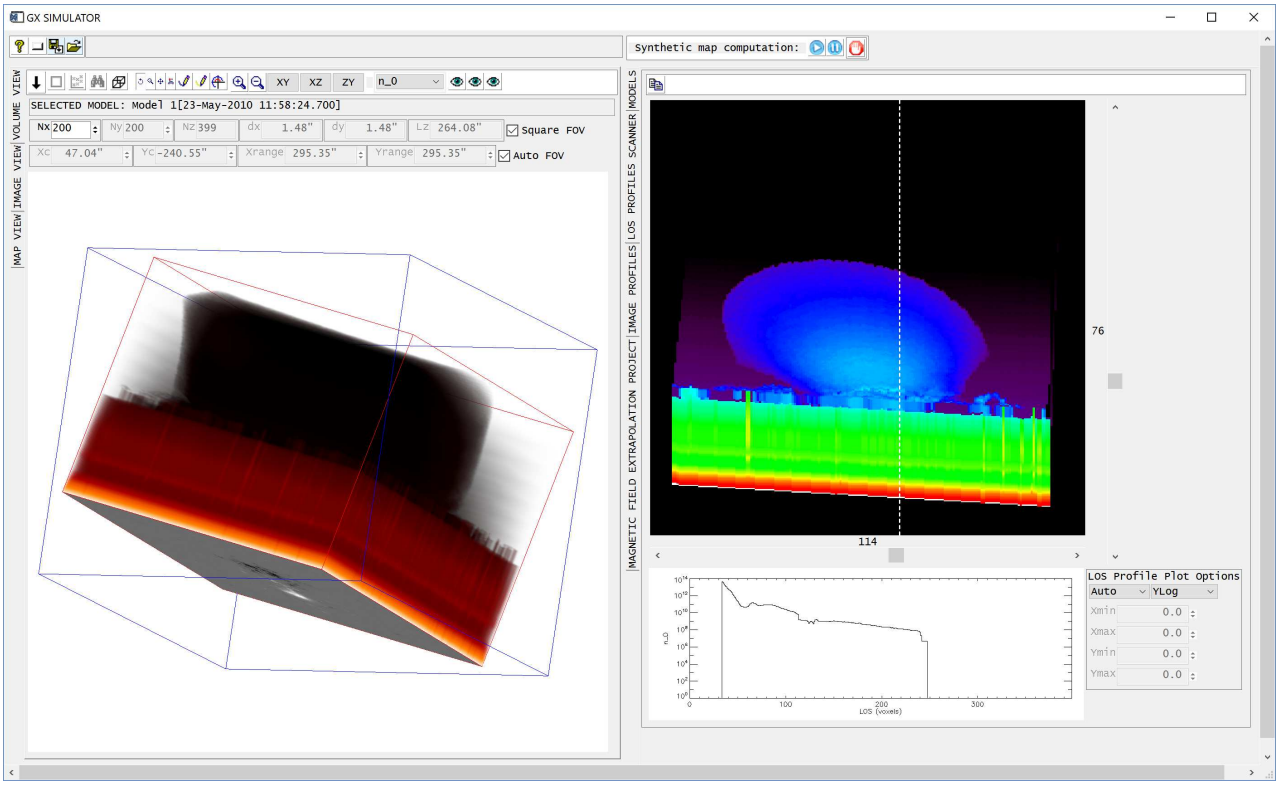

FIG. 3.— Snapshot of the `GX_Simulator` graphical user interface illustrating the electron density distribution corresponding to a composite chromo-coronal model. On the left side the interface displays 3D view of the electron density distribution, and on the right side a 2D slice of the same distribution, which is cut along the observer's line of sight (LOS) direction. The panels are displayed on logarithmic scale.

To illustrate the result of this operation, Figure 3 presents a snapshot of the GX_Simulator graphical interface that displays a 3D view of the electron density distribution on the left, and a 2D slice of the same distribution, which is cut along the observer's line of sight (LOS) direction, on the right. As described above, this composite model is characterized by an irregular vertical grid in the chromospheric volume and a regular grid in the coronal volume that adds up to the same total model height. However, for illustration purposes, to resolve the chromospheric layer, the GX_Simulator interface represents the volume and the LOS slices as equal height layers, which in this case expands the relative height of the chromospheric volume from the true physical ratio of 2:99 to an apparent ratio of 91:99. In Figure 3, the red rectangular box visible on the left side of the snapshot marks the model boundaries, while the blue rectangular box marks the image FOV and LOS direction along which the GX_Simulator renders the volume to compute radiation transfer solution for a given wavelength. In the illustration shown on the right side of Figure 3, the white dotted line marks one such LOS, and its corresponding density profile is shown on the plot below the image of the volume slice. The irregular grid of the chromosphere, as well as the variable height of the TR interface between the two sections of the composite model are also evident in this snapshot.

3.6. *Irregular Grid Rendering*

To solve the radiation transfer equation along an arbitrarily oriented LOS, the current version of GX_Simulator uses a geometrical rendering method that exactly computes the entry and exit points of a given LOS corresponding to each voxel in the original model intersected along its path, and returns a list of irregular segments whose middle points and variable lengths, in combination with the fixed synthesized image pixel size, are used to form new volume elements aligned along the LOS. The physical properties of these new voxels are assigned by means of interpolation based on the physical properties defined in the center of each voxel. To properly take into account the regular nature of the coronal grid and the highly irregular nature of the grid defining the chromosphere, GX_Simulator uses trilinear interpolation in the coronal volume, while for the chromosphere volume, the nearest sample interpolation method is used. This approach has been adopted to avoid the so-called "interface leakage" artifacts that may arise from interpolating across the boundaries between the regions corresponding to different chromosphere models, which results in nonphysically sharp gradients. For similar reasons, instead of interpolated values, center-voxel values are also assigned to all LOS segments located in the vicinity of the transition layer separating the chromosphere and corona. This approach also automatically avoids any non-physical interpolation of certain voxel properties that are shared by all voxels belonging to the same region, but do not have a continuous variation across region boundaries (e.g. integer indexed distribution types or energy spectrum power law slopes, Fleishman & Kuznetsov 2010).

From a technical point of view, GX_Simulator relies on a volume labeling scheme that assigns 64–bit integer voxel IDs, where each binary bit is used to flag the belonging of a given voxel to a particular sub-volume domain. Note that GX_Simulator is designed to model the multi-wavelength emission not only from active regions, but also from flaring loops (Nita et al. 2015). To continue supporting this functionality, the current version generalizes the approach described above by assigning shared unique IDs not only to the chromosphere, transition region, and coronal voxels, but also to any compact region of the model, such as a flaring loop object. This bitwise labeling scheme allows GX_Simulator not only to flag a particular voxel as being located in the chromosphere (bit 1 set), transition region (bit 2 set), or corona (bit 3 set) but, at the same time, as belonging to a particular magnetic flux tube that expands in all these volume regions, which may be uniquely identified by turning on any of the not yet assigned upper bits of the voxel ID. These IDs are then used by the geometrical rendering routine to detect any transitions from one compact region to another, and thus inhibit nonphysical interpolation across adjacent object boundaries.

With this modeling framework we can (1) construct many different plasma models by varying the assumed parameters of the coronal heating; (2) generate synthetic images and spectra representing observations from a variety of existing and future instruments; and (3) compare them with actual observations to "close the loop" of the model-to-data comparison, from which to adjust the heating parameters toward an improved match.

4. COMPARISON OF THE MODEL WITH THE DATA

4.1. *Computation of EUV Emission from the Corona and Transition Region*

While our approach to compute radio and X-ray emission is described elsewhere (Nita et al. 2015; Wang et al. 2015, and references therein), the need to compute EUV emission from the DEM brings new features to the computation, which are described below.

The EUV intensity is computed by convolving the differential emission measure distribution from the model with the appropriate temperature response function, $G(T)$, of the instrument of interest, e.g., AIA:

$$I = \int DEM(T)G(T)dT, \tag{3}$$

assuming either an impulsive or a steady-state heating model.

Our impulsive heating model considers nanoflares that occur randomly within thin, spatially unresolved strands. We assume that the magnitudes of the nanoflares differ depending on the length and average field strength of the strand, but that they are the same for all of the strands passing through a given voxel. We further assume that the strands are so numerous that the time averages (for the coronal and TR portions of the strand, respectively) of a single

nanoflare simulation is equivalent to an instantaneous snapshot of the many out-of-phase strands in a voxel.

The nanoflares used to produce our lookup table have a triangular heating profile of amplitude Q_0 corresponding to our reference values of $B = B_0 = 100$ G, $L = L_0 = 10^9$ cm, and duration $\Delta t = 20$ s. They repeat every $\tau = 10,000$ s. The time-averaged heating rate (for the same reference B and L values) is therefore

$$\langle Q_0 \rangle = \frac{1}{2} Q_0 \frac{\Delta t}{\tau}; \tag{4}$$

thus, after time-averaging, Equation (1) receives the form:

$$\langle Q \rangle = \langle Q_0 \rangle \left(\frac{B}{B_0} \right)^a \left(\frac{L}{L_0} \right)^b. \tag{5}$$

For the steady-state heating model, we assume a sequence of very frequent but weak heating events, so the result does not depend on the actual values of Δt and τ, providing $\langle Q_0 \rangle = Q_0$. In the tool, and hereafter, we use Q for $\langle Q \rangle$ and Q_0 for $\langle Q_0 \rangle$, for brevity.

To account for the coronal contributions to the EUV intensity in a given passband, given the optically thin character of EUV emission (i.e., intensity of emission from each voxel is a product of the emissivity and the voxel volume), we simply add up contributions from all coronal voxels (using the voxel IDs) along the line of sight. Adding the TR contribution, however, requires additional manipulations.

EBTEL does not provide the thickness of the TR, but instead yields the DEM integrated over the (unspecified) TR depth. Therefore, we put all of the TR plasma in the first layer of voxels above the chromosphere. This is reasonable, since the TR is known to be very thin ($\sim 100 - 200$ km), although the upper part of the TR likely extends above this layer in reality. The DEM of a patch of transition region of area $A_{\rm surf} = dxdy$ is proportional to the cross-sectional area of the loop that intersects the patch, $A_{\rm loop} = D_{\rm loop} dy = A_{\rm surf} \cos\theta$, as shown in Figure 4. Since EBTEL computes the DEM for a unit cross-sectional area (1 cm^2) normal to the strand, the output must be multiplied by $A_{\rm surf} \cos\theta$ to obtain the DEM of the patch, where θ is the inclination of the magnetic loop leg with respect to vertical, see Figure 4.

Another correction comes from the fact that the TR thickness is much less than the voxel size, $\Delta \ll dx$, so it is unresolved by our grid. This implies that we have yet to account that the actual volume of the TR segment inscribed by the corresponding voxel depends on the viewing angle. Indeed, the EUV emission from TR is optically thin, thus, it is a product of the emissivity and the contributing volume along the LOS.

This volume is by a factor $1/\cos\varphi$ larger for the actual viewing angle φ relative to the TR plane, compared with the normal viewing angle. Note that this factor does not explicitly depend on the TR thickness Δ given that the EBTEL provides the depth-integrated DEM for the TR. Thus, the intensity of EUV emission, produced from a voxel containing the model TR with the DEM taken from the EBTEL lookup table, must still be multiplied by the geometrical factor $A_{\rm pix} \cos\theta / \cos\varphi$, where $A_{\rm pix} = D_{\rm pix}^2$ is the area of the pixel in the image plane in cm^2, see Figure 4.

However, this form assumes that the transition region is a plane, and the correction factor becomes arbitrarily large for viewing angles approaching 90°. In reality, the curvature of the Sun limits the size of the correction. To make this correction we introduce a φ_0 such as if $\cos\varphi < \cos\varphi_0$ we use $\cos\varphi_0$ instead of $\cos\varphi$. The solution is not sensitive to the exact value of φ_0 and it is only necessary that $\cos\varphi_0$ is reasonable small. To make our selection of φ_0, we note that for a "sliding" LOS, bigger and bigger TR volume would contribute to emission, which can include many TR voxels along such LOS. In the current implementation of the tool, if the given LOS intersects more than one TR voxels, we only account contribution from the one closest to the observer. Thus, to account for the actual intersection of more than one voxel we have to allow $\cos\varphi_0$ to become small enough to describe lines of sight longer that one voxel size. The upper limit to the LOS length along all TR voxels comes from simple spherical geometry considerations, as demonstrated in Appendix B. Thus, taking in consideration the solar radius R and the voxel height dz, we adopt

$$\cos\varphi_0 = \sin\left[\frac{1}{2} \arccos\left(1 - \frac{dz}{R} \right) \right] \tag{6}$$

which, for a typical voxel height of $dz \approx 1000$ km, gives $\cos\varphi_0 \approx 0.027$. Accordingly, we modify the correction factor to have the form $A_{\rm pix} \cos\theta / \max(\cos\varphi, \cos\varphi_0)$.

In addition to these geometrical factors, we also have to account for the inability of NLFF reconstructed magnetic field to correctly reproduce the field inclination at the bottom, non-force-free region of the active region. On the real Sun, photospheric and sub-photospheric dynamics cause the field to be much more vertical in the photosphere compared to the extrapolation model. It flattens out rapidly with height above strong field regions to form a "canopy" of nearly horizontal field at low altitudes in the surrounding weak field regions (Giovanelli 1980; Klimchuk 1987). As discussed above, transition region emission is greatly reduced ($\cos\theta$ factor) in places where the field is approximately horizontal. To account for the limitations of the extrapolation model, we introduce a "canopy" mask and set the transition region emission to zero in the magnetic canopy, which we define as places where the photospheric magnetic field is weaker than a user-defined threshold. This threshold is a free parameter of the model, which is determined based on comparison with EUV data. This approach is tested and validated in Appendix A.

4.2. *Comparison of the Synthesized and Observed Images in the EUV Domain*

To quantify the ability of our modeling framework to reproduce observations, we generated synthetic EUV and MW images from a composite chromosphere-TR-coronal model of AR11072 on

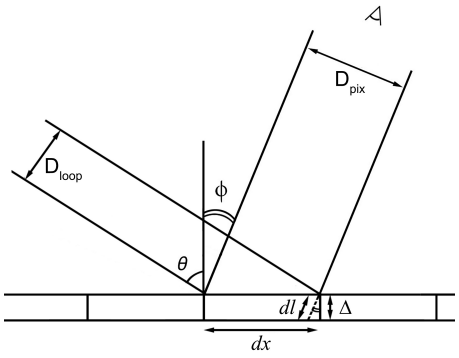

FIG. 4.— Relationship between a loop cross section, D_{loop}, its projection onto the plane of the sky, D_{pix}, and the horizontal voxel sizes, dx and dy, which is the voxel size in the direction normal to the picture plane (not shown in the figure). The axis of the loop and the line of sight are inclined by the angles θ and, respectively, φ, relative to the normal to the transition region layer, which is assumed to have the depths Δ and, respectively, dl, along the normal and line of sight directions.

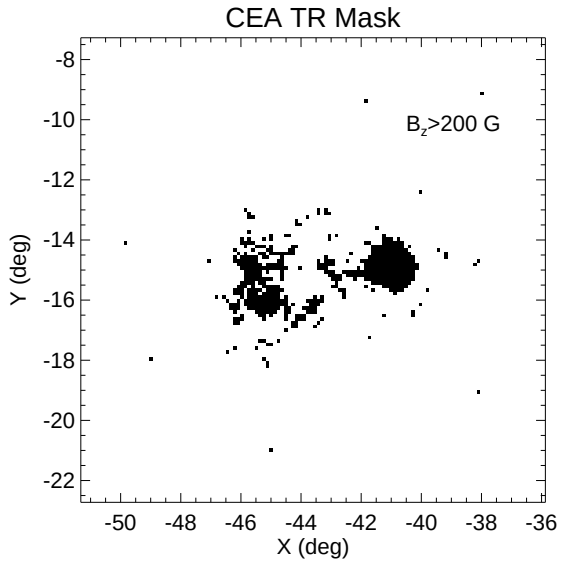

FIG. 5.— Transition Region EUV emission mask obtained by using a vertical component of the photospheric magnetic field threshold of $|B_z| = 200$ G.

2010-May-23, and compared them with imaging observations produced by SDO/AIA at 94, 131, 171, 193, 211, and 335 Å, Nobeyama Radio Heliograph (NORH) at 17 GHz, and the Siberian Solar Radio Telescope (SSRT) at 5.7 GHz. As described in the previous sections and in Appendix A, having the chromospheric model fully constrained by the HMI photospheric input, the only adjustable free parameters remaining to be tuned for finding the best possible agreement between the model and data are the mean heating rate constant, which we set to $Q_0 = 10^{-3}$ erg cm^{-3} s^{-1}, and the TR EUV emission mask threshold, which, as shown in Figure 5, we set to $|B_z| = 200$ G. In what follows we do not fine tune these free parameters, but rather use the specified "round" number for demonstration purposes.

Figure 6 illustrates the comparison between the EUV synthetic maps obtained assuming impulsive and steady-state heating EBTEL models, both computed using the same characteristic mean heating rate, $Q_0 = 10^{-3}$ erg cm^{-3} s^{-1}. The first column displays the observed AIA maps in six wavelength channels. The second and third columns display the synthetic maps produced by `GX_Simulator` using the impulsive and steady-state heating models, respectively, and the fourth and fifth columns display the corresponding model-to-data relative residuals clipped to the ±100% range. Given that we currently employ the lookup tables obtained from time-averaged EBTEL runs, the observational AIA maps used as reference were obtained by averaging the AIA data for a 6-hour interval centered on the time of the NLFFF magnetic extrapolation.

The synthetic images reproduce the bright TR contribution reasonably well, as well as the diffuse component in the AR core, where most of the closed field lines are located. However, neither of the heating models is able to reproduce all loop-like brightness features present in the data. There are two main reasons for that. The first of them is the intrinsic peculiarity of our current implementation of the EBTEL modeling, which does not assign DEM arrays to voxels that are associated with open field lines, including those "truly" closed field lines that do not, however, close within the boundaries of the extrapolation cube. The second one is some unique dynamics leading to a stronger heating of a loop subset, which often stand out clearly in AIA images, that is not captured in the parametrization we currently use. Within the nanoflare framework, loops involve a collective behavior (a nanoflare storm) that is not included in Equation 1 (Klimchuk 2015).

From a quantitative point of view, the relative residual maps shown in the right two columns of Figure 6 indicate that, in most of the channels, and for both heating models, the synthetic emission locally overestimates the observed emission associated with the core AR brightness features, though for most of the image pixels the relative residuals range within reasonable limits of a few tens of percent.

The correspondence of the model to the data in the core region (where the magnetic model captures the closed magnetic field lines) could have been further improved by adjusting the volumetric heating rate parameter Q_0, rather than using the adopted "round" number. However, our model intrinsically underestimates contribution from the FOV periphery due to the lack of the closed field lines there. We thus conclude that, given its self-imposed limitations, our modeling approach is able to satisfactorily reproduce the AIA observations. We note that we could have succeeded in obtaining a better EUV model-to-data spatial match than the one shown here, by employing a position-dependent heating factor capable of generating selective heating of the magnetic structure, which is in principle allowed by the current version of the `GX_Simulator`.

4.3. *Comparison of the Synthesized and Observed Images in the Radio Domain*

Now we turn to synthesising the radio images from the same model. The `GX_Simulator` radio rendering routines do not accept DEM input. Instead, they require the values of plasma temperature and den-

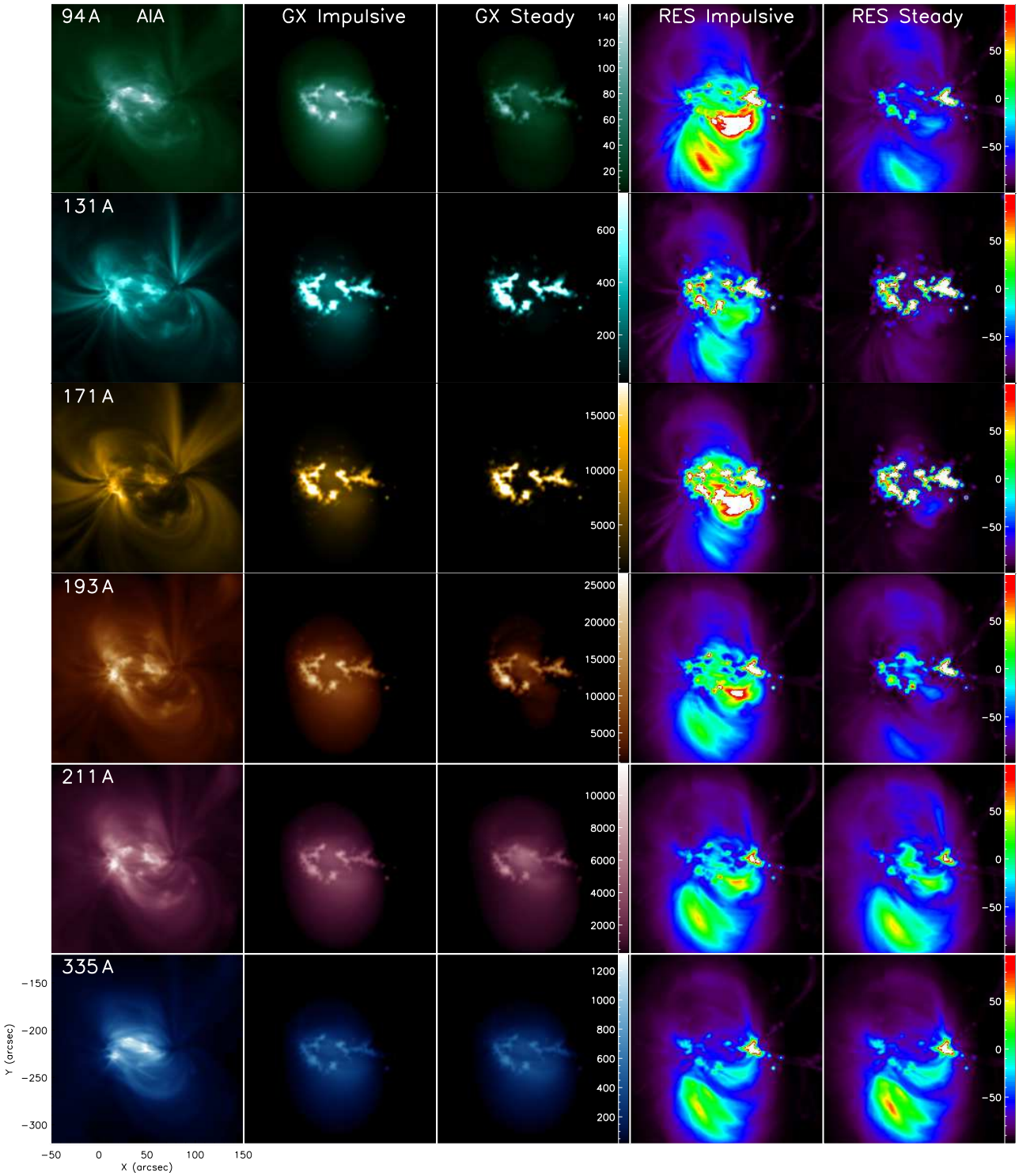

FIG. 6.— EUV synthesized images to observed data comparison for AR 11072 on 23-May-2010. Left Column: SDO/AIA images averaged for a six hour interval centered on the time of the NLFFF magnetic field model. Second column: Synthesized EUV images using the EBTEL impulsive heating DEM solution. Third column: Synthesized EUV images using the EBTEL steady-state heating DEM solution. Both impulsive and steady-state heating models were obtained using the same volumetric heating rate, Equation (5), with $Q_0 = 10^{-3}$ erg cm^{-3}s^{-1}. The images are convolved with circular gaussian beam with $\sigma_x = \sigma_y = 1.2''$. Forth column: Impulsive heating model to data relative residuals clipped to the $\pm 100\%$ range. Right column: Steady-state heating model to data relative residuals clipped to the $\pm 100\%$ range.

sity. For this reason, the radio maps were computed using $n - T$ pairs directly provided in the chromospheric portion of the model by the 1D atmospheres, and computed by Equation (2) in the coronal volume based on the same impulsive (yellow contours) and steady-state (blue contours) EBTEL coronal models used for computation of the synthetic EUV emission discussed above.

Figure 7 demonstrates that our minimal free parameter approach results in a model that is quantitatively consistent with the radio imaging data produced by SSRT at 5.7 GHz (top row) and NORH at 17 GHz (bottom row). In the first column of Figure 7 we display the observed microwave brightness temperature maps (red contours) and the synthesized radio contours, for both steady-state and impulsive models, on top of the HMI LOS magnetic field maps.

Remarkably, for both observed frequencies, the peaks of the brightness temperature maps are reproduced within a few tens of percent accuracy by both heating models, as indicated in Figure 7. The location and morphology of the 5.7 GHz SSRT contours are also matched remarkably well in the simulations. However, the NORH 17 GHz contours indicate a more compact source than in the simulations, as well as a $\sim 20''$ spatial displacement of the emission peak. To assess these spatial and intensity differences quantitatively, we show the absolute brightness temperature residual maps corresponding to the impulsive heating model (middle column of Figure 7) and the steady-state heating model (right column of Figure 7).

5. DISCUSSION

This paper introduces a major upgrade of our modeling tool, `GX_Simulator`, originally developed for 3D flare modeling (Nita et al. 2015). The recently updated tool is now extended to model magnetic and thermal structure of active regions, to generate observables and compare them with data in X-ray, EUV, and radio-to-submillimeter domains. To this end, we developed efficient algorithms of magnetic skeleton reprocessing to fill the skeleton with a realistic distribution of thermal plasma in the chromosphere, transition region, and corona. Because plasma parameters may change abruptly with height in the upper chromosphere and, especially, in the transition region between the chromosphere and corona, we use a non-uniform grid in the vertical direction. Special care has been taken to properly render this non-uniform grid, which can thus be observed from any perspective; not limited to a top view. The proposed approaches are comprehensively tested and validated in Appendix A using a simplified dipole magnetic model.

We then demonstrated the power of this approach by modeling the thermal structure of AR 10072 (2010–May-23) on top of the corresponding NLFFF magnetic data cube. To test the developed model of this AR, we computed synthetic emission from the magneto-thermal data cube in both EUV and radio domains. The quantitative agreement between the synthetic and observed emission integrated over the region is remarkable in both domains, which indicates that the adopted modeling approach is promising. When the spatial distribution is considered, however, we find significant residuals between the synthetic and observed images, which is not surprising given several simplifications adopted. In particular, the time variability of heating and cooling is not explicitly included. In addition, our selected parametric form of the heating function ($a = 2$, $b = -1$) is likely too simplistic. However, with the developed `GX_Simulator` functionality, one can consider other forms of the heating function and add dependence on other parameters available in the model to fine tune the model and, thus, better quantify the coronal heating. In fact, an important use of the tool is to explore various heating parameters in an effort to match observations more closely and thereby better understand the coronal heating mechanism.

6. CONCLUSIONS

We have demonstrated that the tool offers a magneto-thermal structure realistic enough to simultaneously reproduce observables in the EUV and radio spectral domains.

7. APPENDIX A: MODEL VALIDATION

We validate our simulation approach with an idealized bipolar active region, which is much easier to diagnose than a real active region, with all its complexity. We start with a photospheric magnetic flux distribution that corresponds to a horizontal dipole buried below the surface. To mimic the tendency in real active regions for magnetic flux to be concentrated in patches of strong field separated by areas of weak field, we set the field in our model to zero at every location where it is weaker than 600 G. The resulting magnetogram is shown in Figure 8. The "weak field corridor" separating strong positive and negative field is wider than in most real active regions (e.g., Klimchuk 1987), but is useful for testing the model. From this idealized magnetogram, we construct an extrapolated potential magnetic field.

The field is populated with plasma as described in Section 3.3. We consider both steady and impulsive heating. In the steady model, the heating rate varies with the length of the field line (henceforth loop length) according to $Q = Q_0(L/L_0)^{-4}$, where $L_0 = 10^9$ cm and $Q_0 = 10^{-2}$ erg cm^{-3}s^{-1}. The value of Q_0 was chosen to give peak loop temperatures in our computation box that span a range appropriate to real active regions: 1.2-5.2 MK. To avoid enormous heating rates for extremely short loops, GX_Simulator is designed to ignore loops whose length above the chromosphere is shorter than the voxel dimension. This is not an issue for our test case, but can be important for active regions with narrow weak field corridors, or anywhere that opposite polarity fields are in close proximity.

In the impulsive heating model, we assume that nanoflares repeat every 10^4 s. They each have a triangular heating profile lasting 20 s. We let the amplitudes of the nanoflares vary with length in the same way as the steady heating with the same time-averaged heating rate $Q_0 = 10^{-2}$ erg cm^{-3}s^{-1} as in the steady case.

The top panel of Figure 9 shows a synthetic 171 image obtained from the steady heating model. The

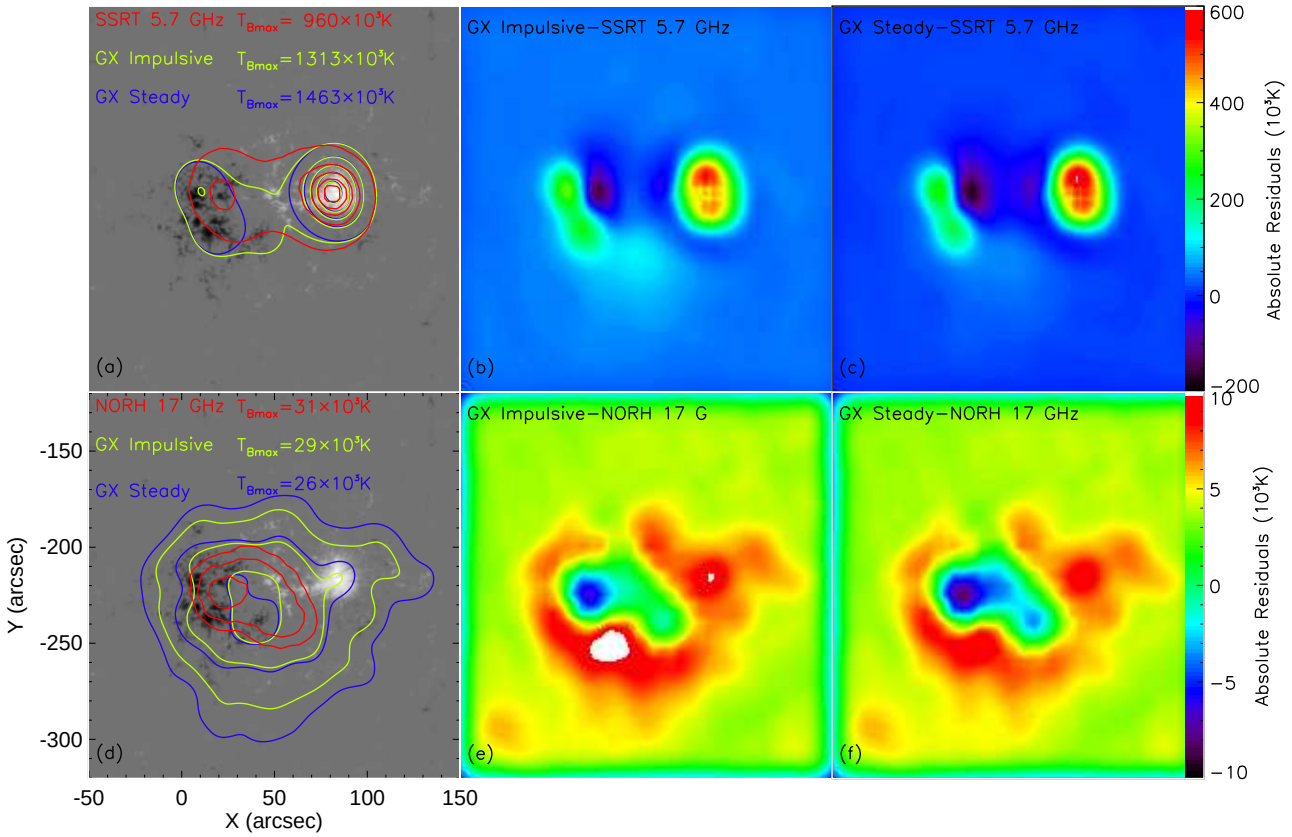

FIG. 7.— AR 11072 23-May-2010 12:00:00 UT: comparison between microwave synthesized images and observations by SSRT at 5.7 GHz (top row) and NORH at 17 GHz (bottom row). a) 10%, 20%,50%,70% and 90% contours of the observed SSRT 5.7 GHz brightness temperature (red contours), impulsive heating (green contours) and steady-state heating (blue contours) synthesized brightness temperature, overlayed on top of the SDO/HMI LOS magnetogram. The plot inset displays the peak brightness temperatures corresponding to the three 5.7 GHz brightness temperature maps, 960×10^3K, 1313×10^3K and 1463×10^3K, respectively. b) Impulsive heating synthetic emission to SSRT 5.7 GHz temperature residual map. c) Steady-state heating synthetic emission to SSRT 5.7 GHz temperature residual map. The same scale in the residual maps shown in panels (b) and (c) is adopted for ease of comparison. d) 55%,70% and 90% contours of the observed NORH 17 GHz brightness temperature (red contours), impulsive heating (green contours) and steady-state heating (blue contours) synthesized brightness temperature, overlayed on top of the SDO/HMI LOS magnetogram. The plot inset displays the peak brightness temperatures corresponding to three 17 GHz brightness temperature maps, 31×10^3K, 29×10^3K and 26×10^3K, respectively. e) Impulsive heating synthetic emission to NORH 17 GHz temperature residual map. f) Steady-state heating synthetic emission to NORH 17 GHz temperature residual map. The same scale in the residual maps shown in panels (e) and (f) is adopted for ease of comparison.

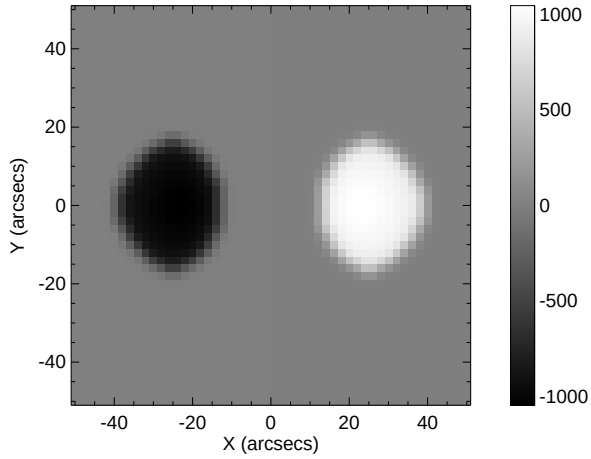

FIG. 8.— Photospheric magnetogram of test case.

vast majority of the emission comes from the transition region footpoints of hot loops. The distribution of the emission is not realistic, however. In real active regions, 171 footpoint emission is confined to areas of bright, reticulated "moss." Moss is spatially well correlated with regions of strong magnetic field in photospheric magnetograms, falling within such regions, often with reduced area, but never outside. Comparing Figures 8 and 9, this is clearly not the case for the model.

The reason for this discrepancy can be traced to the inaccurate nature of the magnetic field model in the photosphere and low chromosphere. The magnetic model is based on a force-free field extrapolation, which assumes that the plasma β vanishes everywhere, although at the bottom (photospheric) boundary the force-free condition does not hold. In other words, there is an abrupt transition from the forced photosphere to a coronal vacuum. For this reason, the NLFFF extrapolated field does not reproduce well the magnetic field just above the photosphere (Fleishman et al. 2017), where large errors of the inclination of the field are likely. This is indicated in the top panel of Figure 10. The real geometry more closely resembles the sketch in the bottom panel of Figure 10.

As discussed in Section 4.1, transition region emission is greatly reduced in places where the field is

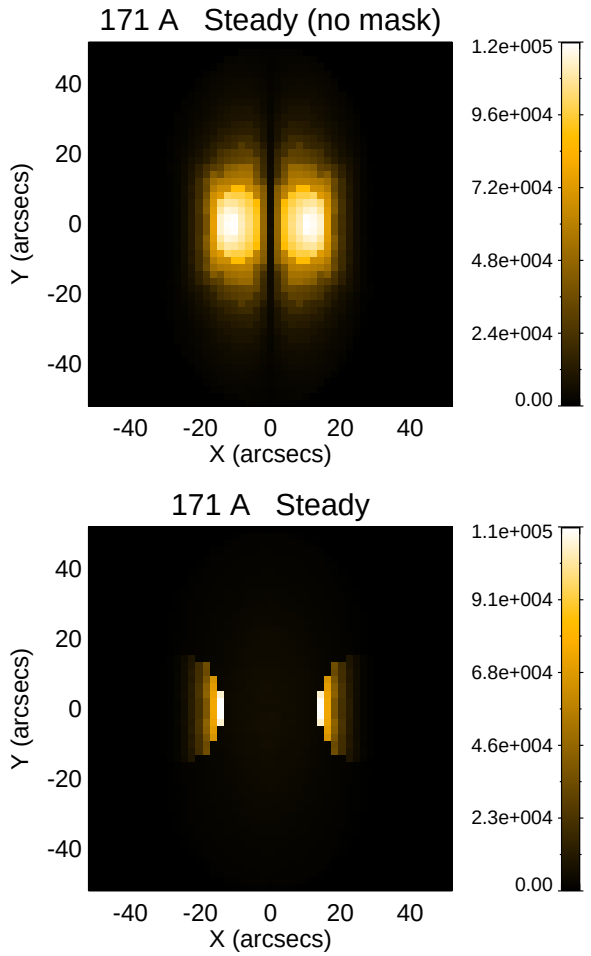

FIG. 9.— Synthetic 171 Å image for the steady heating model without (upper panel) and with (bottom panel) the canopy mask.

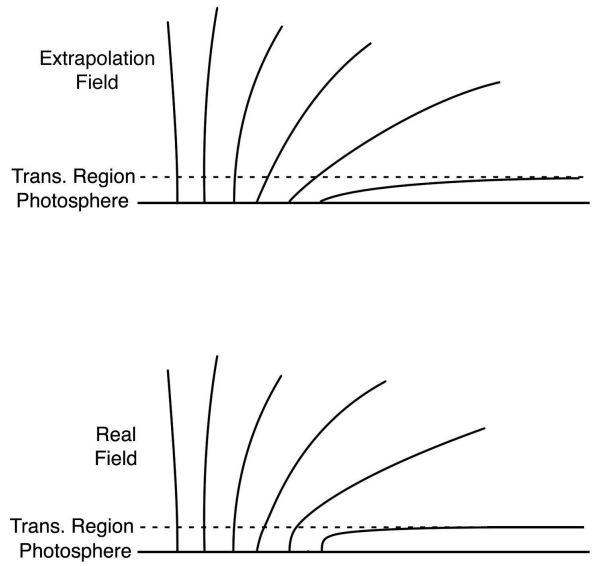

FIG. 10.— Sketch of the magnetic field near the boundary between regions of strong and weak photospheric field for a force-free extrapolation model (top) and the real Sun (bottom).

approximately horizontal, and to account for that, we set the transition region emission to zero in the magnetic canopy. Here, we selected the canopy mask threshold to be 600 G. The bottom panel of Figure 9 shows the corrected 171 Å image when we apply this mask. The correspondence between the image and magnetogram now agrees much better with real observations. The bright moss lies within the strong field regions, and it fades with distance from the central "neutral line" for reasons discussed below.

Figure 11 shows synthetic AIA images in 171, 211, and 94 (left to right) for steady heating (top) and impulsive heating (bottom). The canopy mask has been applied to the transition region in all images. The color table is the same for the both images in each channel so that the brightness differences between steady and impulsive heating are apparent. Recall that the time-averaged heating rates are the same for both models. Figure 12 shows intensity traces across the center of the active region, perpendicular to the neutral line.

Let us first examine the coronal emission for the case of steady heating. It is concentrated in the active region core and is clearly distinguished from the brighter transition region moss emission. As noted above, with steady heating, the maximum loop temperature ranges from 1.2 MK for the longest loops at the active region periphery to 5.2 MK for the shortest loops in the core. The 171 Å channel has peak sensitivity at 0.8 MK and is therefore too cool to show appreciable coronal emission. The 94 Å channel is bimodal, with one peak at 6.7 MK, which is too hot, and another at 1.1 MK, which detects some emission. The 211 Å channel peaks at 1.9 MK and is best suited to the temperature range of the coronal plasma in the model. It shows the greatest emission, both in absolute terms and in relation to the transition region.

It may seem odd that the coronal emission is greatest in the core, even for 211 Å and 171 Å which are better tuned to the cooler temperatures of the longer loops at the periphery. The reason is the density-squared dependence of the emission. In static equilibrium, density varies with temperature and loop length according to $n \propto T^2/L$, where we have assumed a radiative loss function with a $T^{-1/2}$ dependence. The emission measure therefore varies as T^4/L^2. It is much larger for hot, short loops in the core of the active region, and this more than compensates for the decreased temperature sensitivity at core temperatures for 211 Å and 171 Å.

The situation is much different for impulsive heating. Each loop cycles through a wide range of temperatures extending from > 5 MK just after the nanoflare to < 1 MK at the end of the cooling before the next event. Consequently, appreciable coronal emission is present in all of the channels. The brightness depends on the rate at which the plasma cools through the channel's temperature range of greatest sensitivity and on the density of the plasma at that time. Density increases during the initial evaporative phase, when cooling is primarily by thermal conduction, and it decreases during the later draining phase, when cooling is dominated by radiation. Density is great-

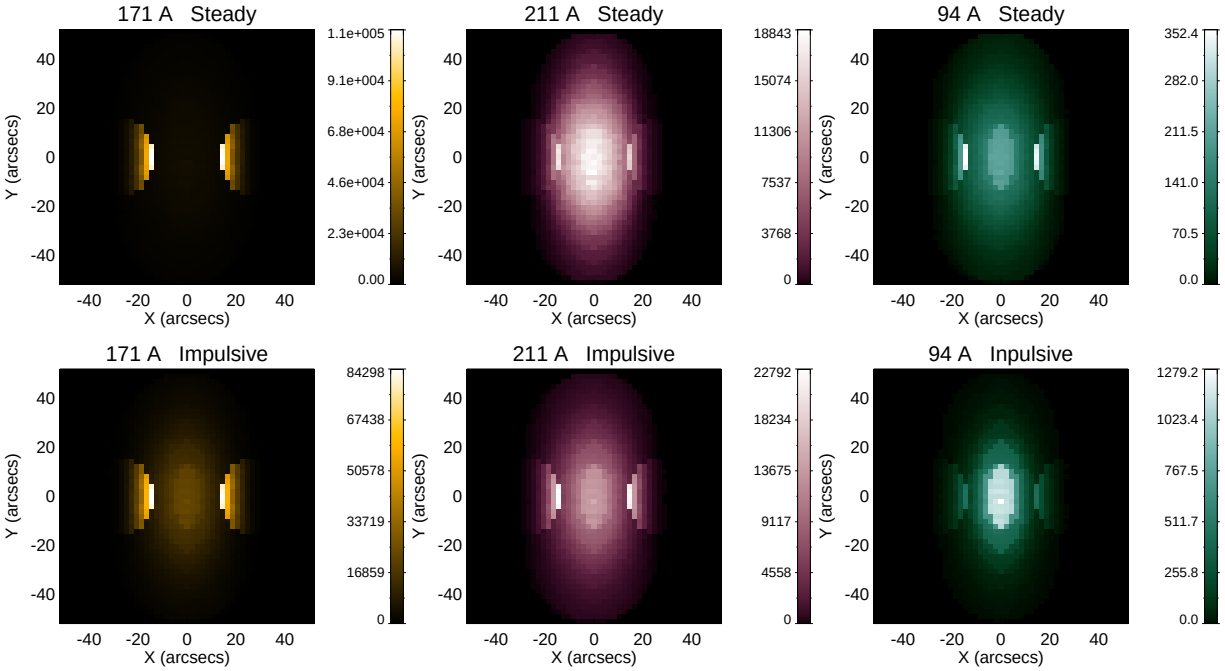

FIG. 11.— Synthetic images in 171 A, 211 A, and 94 A (left to right) for steady heating (top) and impulsive heating (bottom). The canopy masks has been applied to the transition region emission.

est at intermediate times, which is also when the rate of cooling is slowest, so channels that are sensitive to the temperatures that are present at these times have the brightest emission.

Now let us examine the transition region emission in the models. The first thing to note is that it is much stronger than the coronal emission in 171 Å. This is true in real observations as well, though the differences are generally not as great. Impulsive heating provides closer agreement with reality than does steady heating. With impulsive heating, the transition region emission is weaker and the coronal emission is stronger, so the ratio is not as large. This fact was noted by Patsourakos & Klimchuk (2008), who constructed simple arcade models and generated synthetic observations corresponding to a face-on view (a horizontal LOS parallel to the neutral line).

The brightness of the transition region fades rapidly with distance from the neutral line. This is easy to understand, especially for steady heating. As discussed in Klimchuk et al. (2008) (also Viall & Klimchuk (2015)), the brightness of the transition region is proportional to the pressure, which is approximately the same in the transition region and corona of a loop. We have already said that the coronal density varies as T^2/L with steady heating, so pressure varies as T^3/L. Another useful scaling law for steady heating is $T \propto Q^{2/7}L^{4/7}$. But recall that the heating rate we have chosen for the simple models in this Appendix is $Q \propto L^{-4}$, so we find that the pressure varies as $P \propto L^{-19/7}$. This is a strong inverse dependence on length, so we expect the brightness of the transition region to decrease rapidly away from the neutral line in the models.

Given the good agreement of the models with theoretical scalings and with observational trends, we consider them to be fully validated.

APPENDIX B: SPHERICAL GEOMETRY LIMITING FACTOR OF TR CONTRIBUTION ALONG A LINE OF SIGHT

Here we demonstrate our choice for the limiting factor of TR contribution along a line of sight given by Equation 6. As illustrated in Figure 13, due to the spherical shape of the solar surface, there is a maximum number of model voxels n that a given LOS can intersect as it approaches a 90° inclination angle relative to the normal.

Therefore, for inclination angles $\varphi \geq \varphi_0$, as shown in Figure 13, any given LOS would collect surface TR contribution from the same number of voxels $n = l/dx$ as a LOS exactly tangent to the solar surface, which would correspond to $\varphi = 90°$.

Frome simple geometrical considerations, $\varphi_0 = 90° - \psi/2$, thus, $\cos(\varphi_0) = \sin(\psi/2)$.

Hence, taking into account that $\cos(\psi) = 1 - dz/R$, immediately follows that

$$\cos\varphi_0 = \sin\left[\frac{1}{2}\arccos\left(1 - \frac{dz}{R}\right)\right]. \qquad (7)$$

This work was supported in part by NSF grants AST-1615807, AGS-1250374, AGS-1262772, and ICER-1639683, NASA grants NNX14AC87G and 80NSSC18K0015 to New Jersey Institute of Technology, and the RFBR grants 15-02-03717, 15-02-03835, and 16-02-00749. NMV and JAK are supported by the NASA GI and NASA SR programs. We thank our collaborators Sergey Anfinogentov and Alexey Stupishin for useful discussions and providing open access to there codes, including NLFFF reconstruction code, used now by the `GX_Simulator` package. We thank the SDO/AIA team for the use of the AIA data.

REFERENCES

Abramenko, V. I. 1986, Byulletin Solnechnye Dannye Akademie Nauk SSSR, 1986, 83

Alissandrakis, C. E. 1981, A&A, 100, 197

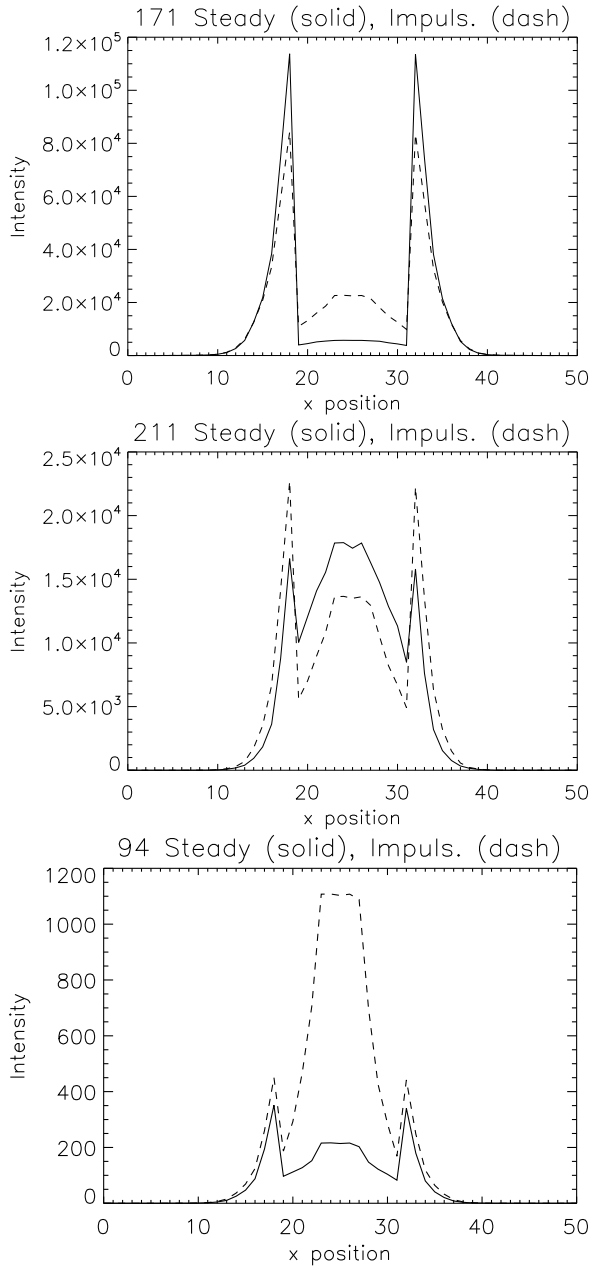

FIG. 12.— Intensity traces across the center of the syntentic maps shown in Figure 11, perpendicular to the neutral line, in the 171 Å, 211 Å, and 94 Å channels (solid–steady heating; dashed–impulsive heating). The canopy mask has been applied to the transition region.

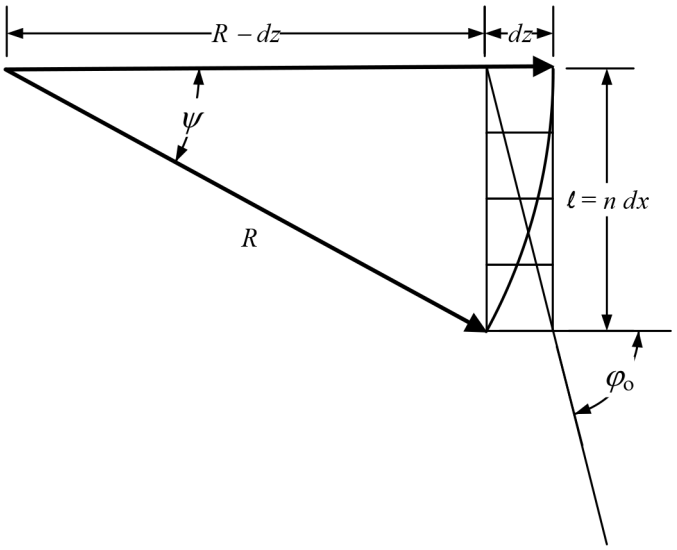

FIG. 13.— Geometry corresponding to a line of sight quasi parallel to the transition region.

Amari, T., Aly, J. J., Luciani, J. F., Boulmezaoud, T. Z., & Mikic, Z. 1997, Sol. Phys., 174, 129
Cargill, P. J., Bradshaw, S. J., & Klimchuk, J. A. 2012a, ApJ, 752, 161
—. 2012b, ApJ, 758, 5
Dahlburg, R. B., Klimchuk, J. A., & Antiochos, S. K. 2005, ApJ, 622, 1191
Daughton, W. S., et al. 2009, AGU Fall Meeting Abstracts
Fleishman, G. D., Anfinogentov, S., Loukitcheva, M., Mysh'yakov, I., & Stupishin, A. 2017, ApJ, 839, 30
Fleishman, G. D., & Kuznetsov, A. A. 2010, ApJ, 721, 1127
—. 2014, ApJ, 781, 77
Fleishman, G. D., & Toptygin, I. N. 2013, Cosmic Electrodynamics. Astrophysics and Space Science Library; Springer NY, Vol. 388, Cosmic Electrodynamics (Springer NY)
Fontenla, J. M., Curdt, W., Haberreiter, M., Harder, J., & Tian, H. 2009, ApJ, 707, 482
Gary, G. A. 2001, Sol. Phys., 203, 71
Giovanelli, R. G. 1980, Sol. Phys., 68, 49
Gudiksen, B. V., & Nordlund, Å. 2005, ApJ, 618, 1020
Hansteen, V. H., Hara, H., De Pontieu, B., & Carlsson, M. 2010, ApJ, 718, 1070
Jing, J., Yuan, Y., Wiegelmann, T., Xu, Y., Liu, R., & Wang, H. 2010, ApJ, 719, L56
Klimchuk, J. A. 1987, ApJ, 323, 368
—. 2006, Sol. Phys., 234, 41
—. 2015, Philosophical Transactions of the Royal Society of London Series A, 373, 20140256
Klimchuk, J. A., Patsourakos, S., & Cargill, P. J. 2008, ApJ, 682, 1351
Lemen, J. R., et al. 2012, Sol. Phys., 275, 17
Malanushenko, A., Longcope, D. W., & McKenzie, D. E. 2009, ApJ, 707, 1044
Mandrini, C. H., Démoulin, P., & Klimchuk, J. A. 2000, ApJ, 530, 999
Mathew, S. K., Martínez Pillet, V., Solanki, S. K., & Krivova, N. A. 2007, A&A, 465, 291
Nita, G. M., Fleishman, G. D., Jing, J., Lesovoi, S. V., Bogod, V. M., Yasnov, L. V., Wang, H., & Gary, D. E. 2011, ApJ, 737, 82
Nita, G. M., Fleishman, G. D., Kuznetsov, A. A., Kontar, E. P., & Gary, D. E. 2015, ApJ, 799, 236
Patsourakos, S., & Klimchuk, J. A. 2008, ApJ, 689, 1406
Peter, H., Gudiksen, B. V., & Nordlund, Å. 2006, ApJ, 638, 1086
Rempel, M., & Cheung, M. C. M. 2014, ApJ, 785, 90
Sakurai, T. 1981, Sol. Phys., 69, 343
—. 1989, Space Sci. Rev., 51, 11
Scherrer, P. H., et al. 2012, Sol. Phys., 275, 207
Selhorst, C. L., Costa, J. E. R., & Silva, A. V. R. 2005, in ESA Special Publication, Vol. 600, The Dynamic Sun: Challenges for Theory and Observations
Tadesse, T., Wiegelmann, T., MacNeice, P. J., Inhester, B., Olson, K., & Pevtsov, A. 2014, Sol. Phys., 289, 831
Thompson, W. T. 2006, A&A, 449, 791
Ugarte-Urra, I., Warren, H. P., Upton, L. A., & Young, P. R. 2017, The Astrophysical Journal, 846, 165
Viall, N. M., & Klimchuk, J. A. 2012, ApJ, 753, 35
—. 2013, ApJ, 771, 115
—. 2015, ApJ, 799, 58
Wang, Z., Gary, D. E., Fleishman, G. D., & White, S. M. 2015, ApJ, 805, 93
Wiegelmann, T. 2008, Journal of Geophysical Research (Space Physics), 113, A03S02